Research article

Tongtong Kang, Zongwei Ma, Jun Qin*, Zheng Peng, Weihao Yang, Taixing Huang, Shilin Xian, Shuang Xia, Wei Yan, Yucong Yang, Zhigao Sheng*, Jian Shen, Chaoyang Li, Longjiang Deng* and Lei Bi*

Large-scale, power-efficient Au/VO_2 active metasurfaces for ultrafast optical modulation

https://doi.org/10.1515/nanoph-2020-0354
Received June 30, 2020; accepted October 24, 2020; published online November 17, 2020

Abstract: Active metasurfaces, in which the optical property of a metasurface device can be controlled by external stimuli, have attracted great research interest recently. For optical switching and modulation applications, high-performance active metasurfaces need to show high transparency, high power efficiency, as well as ultrafast switching and large-scale fabrication capability. This paper reports Au/VO_2-based active metasurfaces meeting the requirements above. Centimeter-scale Au/VO_2 metasurfaces are fabricated by polystyrene sphere colloidal crystal self-assembly. The devices show optical modulation on-off ratio up to 12.7 dB and insertion loss down to 3.3 dB at 2200 nm wavelength in the static heating experiment, and $\Delta T/T$ of 10% in ultrafast pump-probe experiments. In particular, by judiciously aligning the surface plasmon resonance wavelength to the pump wavelength of the femtosecond laser, the enhanced electric field at 800 nm is capable to switch off the extraordinary optical transmission effect at 2200 nm in 100 fs time scale. Compared to VO_2 thin-film samples, the devices also show 50% power reduction for all-optical modulation. Our work provides a practical way to fabricate large-scale and power-efficient active metasurfaces for ultrafast optical modulation.

Keywords: all-optical modulation; metasurface; phase change materials; surface plasmon resonance; VO_2.

***Corresponding authors: Jun Qin, Longjiang Deng and Lei Bi**, National Engineering Research Center of Electromagnetic Radiation Control Materials, University of Electronic Science and Technology of China, Chengdu 610054, China; and **Zhigao Sheng**, Anhui Key Laboratory of Condensed Matter Physics at Extreme Conditions, High Magnetic Field Laboratory, Chinese Academy of Sciences, Hefei 230031, China, E-mail: qinjun@uestc.edu.cn (J. Qin), denglj@uestc.edu.cn (L. Deng), bilei@uestc.edu.cn (L. Bi), zhigaosheng@hmfl.ac.cn (Z. Sheng). https://orcid.org/0000-0002-5456-0850 (J. Qin). https://orcid.org/0000-0002-2698-2829 (L. Bi).
Tongtong Kang, Zheng Peng, Weihao Yang, Shilin Xian, Shuang Xia, Wei Yan and Yucong Yang, National Engineering Research Center of Electromagnetic Radiation Control Materials, University of Electronic Science and Technology of China, Chengdu 610054, China, E-mail: kangtt@std.uestc.edu.cn (T. Kang), 201821020431@std.uestc.edu.cn (Z. Peng), 201921021124@std.uestc.edu.cn (W. Yang), 442437912@qq.com (S. Xian), 201811022306@std.uestc.edu.cn (S. Xia), weiyan@std.uestc.edu.cn (W. Yan), 201921021123@std.uestc.edu.cn (Y. Yang)
Zongwei Ma, Anhui Key Laboratory of Condensed Matter Physics at Extreme Conditions, High Magnetic Field Laboratory, Chinese Academy of Sciences, Hefei 230031, China, E-mail: mazongwei@hmfl.ac.cn (Z. Ma)
Taixing Huang, National Engineering Research Center of Electromagnetic Radiation Control Materials, University of Electronic Science and Technology of China, Chengdu 610054, China; and Sichuan Province Key Laboratory of Information Materials and Devices Application, Chengdu University of Information Technology, Chengdu 610225, China, E-mail: liyaoliyao8@163.com
Jian Shen and Chaoyang Li, State Key Laboratory of Marine Resource Utilization in South China Sea, Hainan University, No. 58, Renmin Avenue, Haikou, Hainan Province 570228, China; and Dongguan ROE Technology Co., Ltd., Dongguan, China, E-mail: shenjian@hainanu.edu.cn (J. Shen), 3134299474@qq.com (C. Li)

1 Introduction

The development of metasurfaces in the past decade has reformed the way we manipulate the light. Metasurfaces are two-dimentional (2D) metamaterials, which control the amplitude, phase and polarization of light at the sub-wavelength scale [1–10]. By carefully designing the shape, location and spacing of meta-atoms, the far-field wave front of the propagating light can be efficiently controlled, creating innovative 2D photonic devices such as flat lens, perfect absorbers, nonreciprocal metasurfaces and nonlinear metasurfaces, just to name a few [1, 2, 4, 5, 11–19]. Besides, metasurfaces are also demonstrated to modulate near-field surface wave or surface plasmon modes [20–24]. Despite of these progresses, most metasurface devices demonstrated today are passive, with fixed optical properties after design

and fabrication. Active metasurfaces, which allow tuning of the optical properties by an external stimulus, have attracted great research interest recently. One way to fabricate an active metasurface is to integrate active photonic materials as part of the meta-atoms. Under electrical [25, 26], magnetic [27], thermal [28, 29] or optical stimuli [30, 31], the optical constants of the active photonic materials can be modulated, leading to modulation of the near-field modal profile, and consequently the far-field optical properties of the metasurfaces. A variety of active photonic materials are proposed for active metasurface applications, such as phase change materials [29, 32, 33], epsilon-near-zero materials [34, 35], liquid crystals [28, 36, 37], magnetooptical materials [27], metals via electrochemical reactions [38] and 2D materials [25, 39]. Novel functionalities based on these devices are also demonstrated, including optical switching and modulation, beam steering, tunable structural color and thermal camouflage, etc [26, 29, 33, 36, 40–45].

Phase change materials, like VO_2, GST, GSST, can provide a large refractive index contrast for active metasurface applications [46–49]. Among these materials, VO_2 has several advantages. First, compared to GST/GSST, devices based on VO_2 require lower energy or temperature to induce the insulator-metal phase transition (IMT) [46]. Second, the IMT of VO_2 is volatile, so it can be used for devices requiring dynamic modulation. Third, the IMT process of VO_2 can be triggered in the femtosecond time scale by photon excitation. This ultrafast IMT process is attributed to a Mott-Hubbard type phase transition caused by photocarriers induced Mott band gap collapse without crystal structural change [50–52]. A recent experiment shows such a phenomenon takes place within 30 fs [53]. Therefore, VO_2 has been recognized as a promising phase change material for active metasurface applications. VO_2 shows IMT at the temperature of 68°C [54–56], accompanied with significant optical constant variation in the visible to THz frequency range. Various VO_2-based active nanophotonic devices have been developed for applications including tunable polarizers [57], all-optical switching [58–61], tunable structural colors [62], adaptive camouflage and tunable perfect absorbers [63], etc. Energy-efficient phase transitions have been observed in Au/VO_2 hybrid plasmon structures [56, 64, 65]. However, many of these devices show relatively low transmittance due to high loss plasmonic resonance modes such as localized surface plasmon resonance [56, 65], which is not desired for optical modulation. Besides, VO_2-based plasmonic devices usually require expensive top-down fabrication methods such as electron-beam lithography and focused ion beam etching, limiting the device size to small areas.

Here, we report fabrication and characterization of a large-scale, power-efficient Au/VO_2-based active metasurface for ultrafast optical modulation applications. Using a bottom-up self-assembly method, we fabricated centimeter-scale Au/VO_2-based active metasurfaces showing unprecedented high device performance compared to similar structures reported before. The device shows a high on-off ratio up to 12.7 dB and low insertion loss down to 3.3 dB at 2200 nm wavelength in the static heating experiment, based on the extraordinary optical transmission (EOT) effect. We also demonstrate ultrafast all-optical switching capability by femtosecond laser excitation. All-optical switching amplitude up to $\Delta T/T = 10\%$ is observed in the femtosecond time scale at the highest transmission wavelength of 2200 nm. Compared to VO_2 thin films, up to 50% optical switching power reduction is observed both in the femtosecond and picosecond time scale. This is achieved by judiciously aligning the Au surface plasmon resonance excitation wavelength with the pump laser wavelength at 800 nm, achieving efficient plasmon enhanced light absorption and hot-electron injection in VO_2 in the femtosecond time scale, as well as plasmon enhanced photothermal effect in the picosecond time scale. Both mechanisms lead to efficient IMT of VO_2 and all-optical modulation of the metasurfaces.

2 Results and discussion

Figure 1A shows a sketch of the device structure. The device consists of a 90-nm-thick VO_2 thin-film layer and a 30-nm-thick perforated Au thin film deposited on a double side polished SiO_2 substrate. The VO_2 thin films are firstly deposited by pulsed laser deposition (PLD) (see Methods). Temperature-dependent Raman spectrum and optical constants measurements showed the crystal structure change and IMT process of VO_2 (see Figure S1 of Supplementary Materials). Then, a monolayer colloidal sphere mask using PS spheres was self-assembled on the VO_2 thin film. Oxygen plasma is used to downscale the size of the PS spheres from 550 nm to 400 nm. Subsequently, Au thin films were deposited on the sample by sputtering, followed by a lift-off process to form the perforated nanohole structure (see Methods and Figure S2 of Supplementary Materials). Figure 1B shows a $20 \times 15\ \mu m^2$ SEM image of the metasurface device. For even larger samples, we present a photograph of a $2 \times 2\ cm^2$ metasurface sample fabricated by self-assembly, as shown in Figure 1C. We can apparently observe the diffracted light of the sample, which means the formation of periodic structures like in Figure 1B. We see different colors with mosaic pattern on the scale of millimeters across the sample. This is due to different azimuth angles between different locations of the periodical structure shown in Figure 1B, which shows different colors for glanced incidence [66]. Although inhomogeneity is observed in large-scale, the optical

transmittance spectrum is homogeneous across the sample under normal incidence (see Figure S3 of Supplementary Materials). The Au nanoholes form a hexagonal lattice structure, with hole diameter of $d = 390 \pm 10$ nm and hole period of $p = 550 \pm 50$ nm, resembling the reverse pattern of the self-assembled PS spheres. The period has a larger standard deviation because the PS spheres are relatively displaced from the periodical lattice during the fabrication process (see Figure S4 of Supplementary Materials). Figure 1D shows surface morphology of the metasurfaces measured by atomic force microscopy (AFM). The surface root-mean-square (RMS) roughness of the Au thin film at flat areas is 1.5 nm, indicating a smooth Au thin film deposited on VO_2 thin films. The optimization and design process of the device is shown in Figure S5 of Supplementary Materials.

To demonstrate the optical modulation properties, we first characterized the temperature-dependent transmission spectrum of the metasurface samples. The measurement results are shown in Figure 2A and B. The static transmittance curves are normalized to air. The bare SiO_2 substrate shows transmittance of 90% at around 2000 nm wavelength. For comparison, control samples with only VO_2 thin films deposited at the same time on quartz substrates were also measured, as shown in Figure 2C and D. Both samples were measured for the heating and cooling process. As varying the device temperature between 30–80°C, we notice significant modulation of the transmittance spectrum in the near infrared for both samples due to the IMT process in VO_2. Three major differences are observed. First, in the wavelength range of 750–1250 nm, the metasurface sample shows much lower transmittance compared to the control sample. This corresponds to the excitation of the SPR mode, which enhances the electric field at the interface between the metal and VO_2 film. Second, at around 2200 nm wavelength, a maximum transmittance is observed in the metasurface sample. Despite of a gold thin film on the metasurface device, the sample shows only slightly lower transmittance compared to the bare VO_2 thin film, showing a low insertion loss of 3.3 dB. This wavelength corresponds to the EOT effect as observed in periodic plasmonic nanohole structures, where SPR modes are excited and hybridized on both surface of the perforated Au film. The SPR modes couple to radiation modes [67–70], leading to a low transmission loss [71, 72]. Third, the off state of the metasurface devices shows much lower transmittance compared to the VO_2 thin film across the whole near infrared wavelength range. This can be better observed in Figure 2E, which shows the optical transmittance hysteresis at 2200 nm as a function of temperature. Both samples show similar IMT temperature range between 30 and 80°C. A clear increase of the on/off ratio for the metasurface sample can be observed from this figure. In static heating experiment, the extinction ratio of the metasurfaces reaches 12.7 dB, whereas the thin film sample reaches only 7.8 dB. To better show the difference between the metasurfaces and the VO_2 thin-film samples, we simulated the modulation depth of VO_2 films with different thicknesses, as shown in Figure 2F. Here, the thickness of VO_2 films varied from 90 to 150 nm. We extracted the transmission loss at 2125 nm wavelength both for the metallic and the dielectric states and compared with the metasurface sample, as shown in Figure 3A. We notice higher loss in thicker VO_2 films (above 120 nm) in the dielectric state, as well as a lower extinction ratio until the VO_2 film thickness reaches above 150 nm. Therefore, a higher on/off ratio is always achieved in the metasurface sample, despite the VO_2 is the thinnest (90 nm).

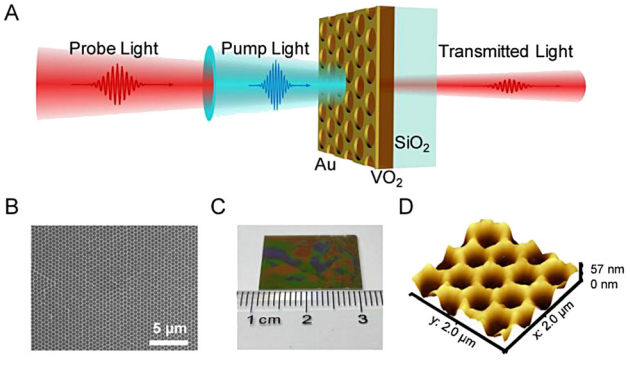

Figure 1: Design and fabrication of the Au/VO_2 active metasurfaces. (A) Sketch of the VO_2-based active metasurface device. An 800-nm wavelength femtosecond pump light (blue) is used to trigger the IMT of VO_2, which is probed at around 2200 nm wavelength. (B) Top-view SEM image of the metasurface showing a 20×15 μm^2 size area. (C) Photograph of 2×2 cm^2 active metasurface sample. (D) AFM surface morphology of the Au/VO_2 metasurfaces.

To understand the optical modulation mechanism, we used finite element methods (COMSOL MULTIPHYSICS®) to simulate the transmission spectrum and modal profiles. The optical constants for VO_2 at this wavelength range are characterized by ellipsometry (J. A. Woollam). In the simulations, light incidents from the Au thin film side with polarization along the y axis, as shown in Figure 3A. Figure 3B shows the simulated and experimental transmission spectra of the metasurfaces for the dielectric and metallic states, respectively. The simulation quantitatively matches well with the experimental results measured at both dielectric and metallic states. From Figure 3B, we observe a transmittance dip around 1000 nm and peak around 2200 nm, as the star markers shown. There is a small difference of the peak wavelength between experiment and simulation, which may be resulted from the

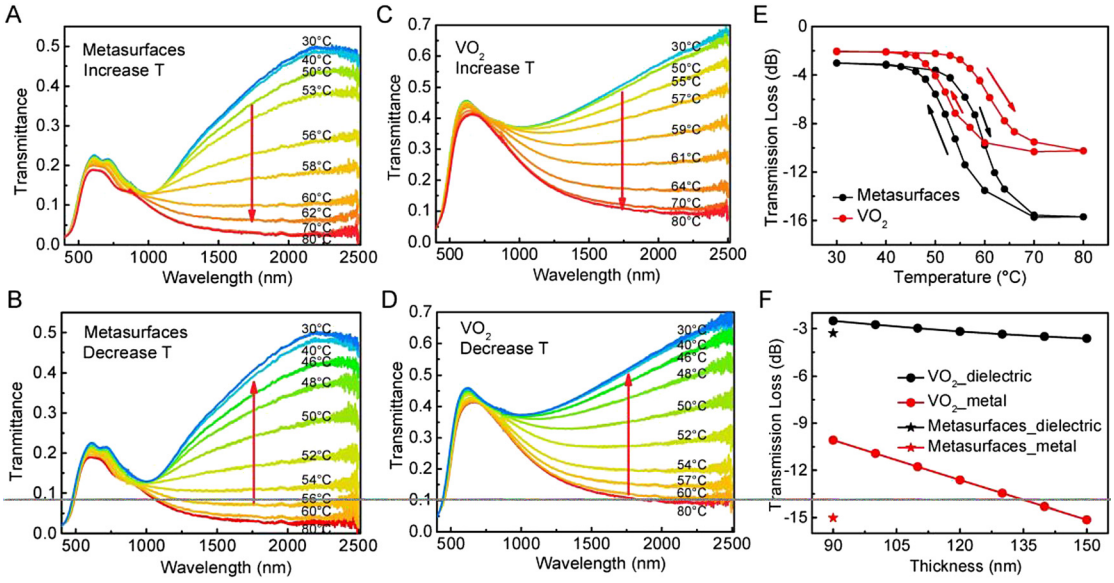

Figure 2: Temperature-dependent transmittance spectra of the metasurfaces for (A) increasing temperature and (B) decreasing temperature, respectively. Temperature-dependent transmission spectra of VO_2 thin films for (C) increasing temperature and (D) decreasing temperature, respectively. (E) Transmittance of the metasurfaces and the VO_2 thin film as a function of temperature at 2200 nm wavelength. (F) Simulated transmission loss as function of VO_2 thickness for VO_2 films and Au/VO_2 metasurfaces.

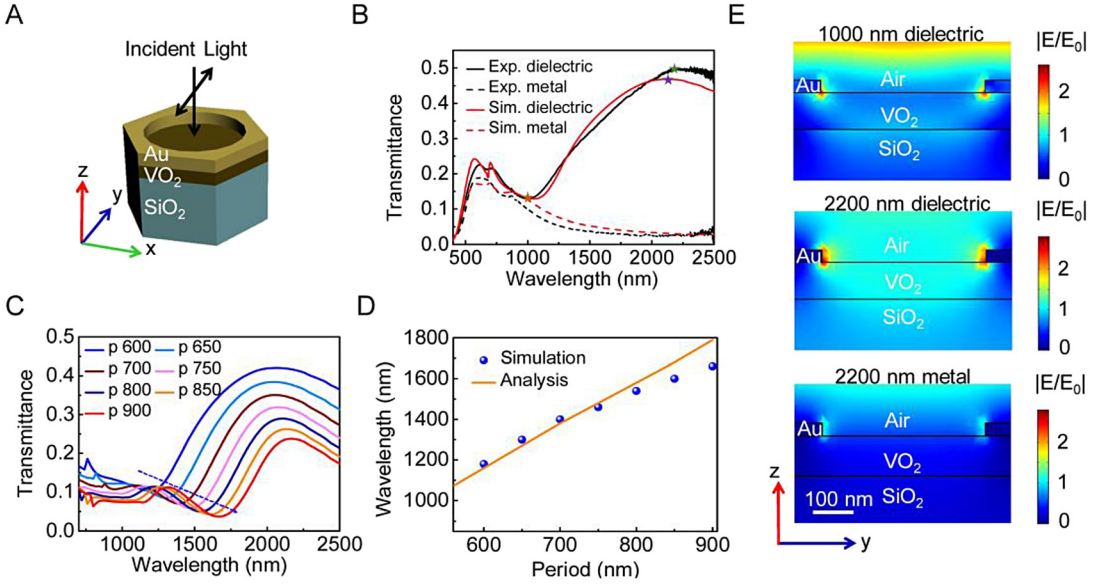

Figure 3: Far-field and near-field analysis of the metasurfaces.
(A) Schematic of the periodic unit cell for our simulation. (B) Simulated and experimental transmittance spectra at dielectric and metallic state. (C) Simulated transmittance spectra with period changing from 600 to 900 nm. (D) Resonant wavelength of SPR as a function of period for simulation and analytic method. (E) Electric field distributions of an SPR mode, EOT at a dielectric state and EOT at a metallic state in *y*–*z* plane, respectively.

different material optical parameters used in our simulation. Firstly, to clarify the resonant mode around 1000 nm wavelength, we simulate the transmittance spectra as a function of period, as shown in Figure 3C. As the period changing from 600 to 900 nm, the dip wavelength shifts to longer wavelength, which is the characteristic of the SPR mode. To further confirm the SPR mode at around 1000 nm wavelength, we use the dispersion relationships for the thin film, which can be derived based on the coupled modes theory [73, 74]:

$$\tanh(\alpha_m t) = -\frac{\epsilon_m \alpha_m (\epsilon_{d1}\alpha_{d2} + \epsilon_{d2}\alpha_{d1})}{\epsilon_{d1}\epsilon_{d2}\alpha_m^2 + \epsilon_m^2 \alpha_{d1}\alpha_{d2}} \quad (1)$$

Where $\alpha_{d1}^2 = k_{sp}^2 - \epsilon_{d1}k_0^2$, $\alpha_{d2}^2 = k_{sp}^2 - \epsilon_{d2}k_0^2$, $\alpha_m^2 = k_{sp}^2 - \epsilon_m k_0^2$ and $k_{sp} = k_0 \sin(\theta)\cos(\varphi) \pm nG_x \pm mG_y$. k_0 is the free-space wavenumber, θ is incident angle, φ is azimuth angle of the polarization, ε_{d1} is the permittivity of the coating dielectric layer (air), ε_{d2} is the permittivity of the cladding dielectric layer (VO_2 and SiO_2) and t is the thickness of Au. We note that ε_{d2} is also different from pure VO_2 as part of the field penetrates into SiO_2. Here, the effective ε_{d2} is around 4.8+i *1.3. Using the same geometric sizes and material parameters as the simulation, we obtain the resonant wavelength by the Equation (1), which is consistent with the simulated results, as shown in Figure 3D. Therefore, the resonance at 1000 nm wavelength is corresponding to the hybrid SPR mode. Secondly, for the resonant peak at around 2200 nm wavelength, the mode also shows a red shift as increasing the periods from 600 to 900 nm, which is the characteristic of EOT effect. For EOT, except for satisfying Equation (1) of the SPR mode, the momentum matching condition between the propagating SPR mode and SPR scattered by the holes also need to be satisfied [75, 76].

$$\left|k_0 \sin(\theta)\cos(\varphi) \pm nG_x \pm mG_y\right| * P + \arg(\tau + \rho) = 2l\pi \quad (2)$$

Where k_0 is the free-space wavenumber, θ is incident angle, φ is azimuth angle of the polarization, $G_{x/y}$ is lattice reciprocal vector equal to $2\pi/P_{x/y}$, P is the period, m, n and l are integers and $\arg(\tau+\rho)$ is the phase shift due to the SPR scattered by the air holes, which is related to the hole size. Therefore, the EOT wavelength will show the same characteristic as SPR mode. The radius dependence is also presented in Figure S6 of Supplementary Materials. In the top of Figure 3E, we simulate the modal profiles of the normalized electric field amplitude $|E/E_0|$ at 1000 nm wavelength, where E_0 is the incident electric filed intensity in free space. The electromagnetic field is mainly concentrated on the edges of Au nanoholes, indicating the excitation of the SPR mode [77]. The modes are plotted in the y-z plane at the center of the hole. Significant field attenuation is observed after propagating through the metasurfaces into the substrate side. In the middle of Figure 3E, for the dielectric state of VO_2, we observe the electric fields concentrating at the Au nanohole edges of the Au/air and Au/VO_2 interface at EOT wavelength. Thanks to the very thin thickness of Au film (30 nm), these two modes couple to each other and radiate through the Au layer, leading to the EOT effect [67–70]. In contrast, when VO_2 is in the metallic state, the SPR mode is much weaker especially at the Au/VO_2 interface. Metallic VO_2 film reflects most of the incident light, and the EOT channel closes, leading to a high extinction ratio of the off state, as shown in the bottom of Figure 3E.

Next, we characterized the ultrafast all-optical modulation properties of the metasurfaces using the pump-probe method. The device was pumped using a Ti:sapphire laser at 800 nm wavelength and probed with an infrared pulse at around 2200 nm wavelength generated by an optical parametric amplifier (OPA) (see Figure S7 of Supplementary Materials). We can see good endurance of the device from the ultrafast pump-probe experiment itself in Figure 4. For these measurements, each point on the plot indicates the average transmittance for 300 times pump-probe experiments at a certain time delay. Therefore, these samples can endure at least 1 million all-optical switching cycles based on these measurements. We also repeated the pump-probe measurements, and the ultrafast modulated transmission spectrum can reproduce itself. At 800 nm wavelength, the pump light excited the SPR, which leads to three consequences, i.e., enhanced optical field and absorption in VO_2, hot carrier injection in VO_2, as well as the photothermal effect. The first two mechanisms took place in the femtosecond time scale, and the third mechanism dominated at longer time of the picoseconds to nanoseconds [78]. Figure 4A and C show the transient modulated transmissivity probed at 2200 nm wavelength for the metasurfaces and the VO_2 thin film, respectively. Transmissivity profile for a longer time is shown in Figure 4B and D. The pump fluences for the metasurfaces and the VO_2 thin film were 2.7 to 13.9 mJ cm^{-2} and 5.3 to 25.2 mJ cm^{-2} respectively. We set this fluence range to be across the threshold fluence F_{TH} of photoinduced IMT in VO_2 of 9 mJ cm^{-2} [50, 79]. Below this threshold, the ultrafast photoinduced response is attributed to a nonthermal transient IMT [50–52], in which the Mott band gap closes due to the photon absorption of VO_2, creating extra holes at the valence band top which modulates the Coulomb interactions. The material structure at this state has been recently characterized by ultrafast electron diffraction as a metastable metallic monoclinic (mM) phase [50–52]. With the carrier cooling and redistribution, the material returns to the insulating monoclinic phase at a longer time scale. In this fluence range, we observed much lower power required to switch the metasurface device compared to the VO_2 thin film. In particular, for achieving 1% transmittance variation, the power required for switching the metasurfaces and the VO_2 thin film was 2.7 and 5.3 mJ cm^{-2} respectively, corresponding to 49% lower pump energy. This phenomenon can be compared with SPR-induced enhancement of the optical field, absorption and photocarrier generation in VO_2. Simulation of the modal profiles

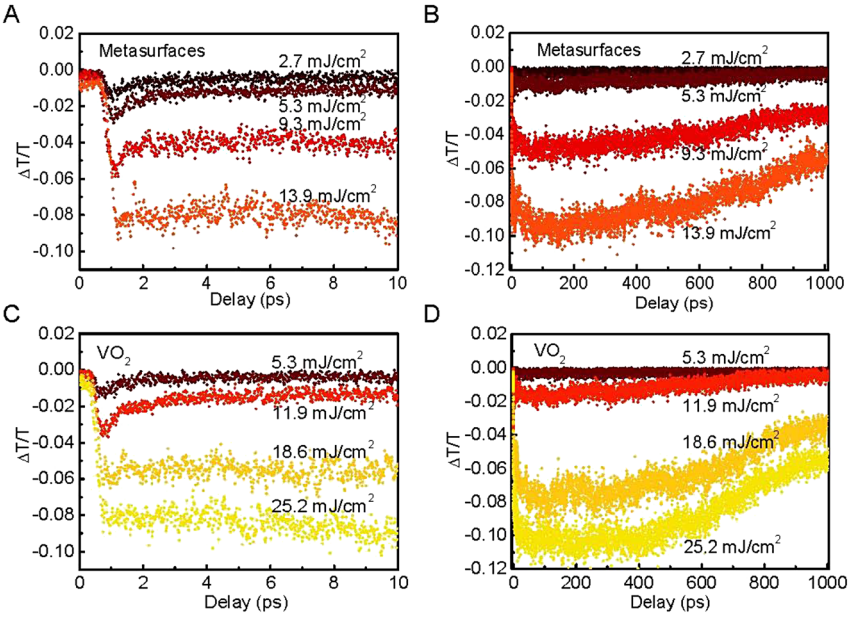

Figure 4: Ultrafast spectral response of the fabricated metasurfaces.
(A) The ultrafast modulated transmittance spectrum of the metasurfaces with pump fluence changing from 2.7 to 13.9 mJ cm^{-2} within 10 ps time scale. (B) The same ultrafast modulated transmittance spectrum of the metasurfaces as Figure 4A within 1000 ps time scale. (C) The ultrafast modulated transmittance spectrum of the pristine VO_2 with pump fluence changing from 2.7 to 13.9 mJ cm^{-2} within 10 ps time scale. (D) The same ultrafast modulated transmittance spectrum of the pristine VO_2 as Figure 4C within 1000 ps time scale.

at 800 nm (see Figure S9A of Supplementary Materials) indicates 1.8 times field enhancement at the Au/VO_2 interface compared with bare VO_2 thin films, which is consistent with the observed fluence difference. Meanwhile, SPR-induced hot-carrier injection is also observed to contribute to the nonequilibrium carrier concentrations in VO_2 in previous reports, which could further reduce the pump energy in the metasurface sample [64, 80].

For fluences above F_{TH}, the photon-induced heating is strong enough to cause structural phase transition of VO_2 from the insulating/metallic monoclinic phase to the metallic rutile phase [45]. For the metasurface sample, this range corresponds to pump fluences of 5.3, 9.3 and 13.9 mJ cm^{-2}, whereas for VO_2 thin films, this range is 11.9, 18.6 and 25.2 mJ cm^{-2}. This scenario is supported by the appearance of a second transmission minimum due to structural phase transition at around 100–200 ps for both samples, as shown in Figure 4B and D. Again, the metasurface sample shows lower all-optical switching fluence. For 10% transmission modulation, the metasurfaces needs 13.9 mJ cm^{-2} fluence, which is 45% less compared to VO_2 thin film of 25.2 mJ cm^{-2}. This trend can be well explained by numerical simulations (COMSOL Multiphysics) by considering the photothermal effect (see Figure S9B of Supplementary Materials). The local electromagnetic field was absorbed by Au and VO_2, which are considered as a heat source during the simulation. The temperature profile at 200 ps can be simulated after 100 fs pump laser pulse radiation at 800 nm wavelength. Compared to VO_2 thin films, the metasurfaces only needs about half of the laser pulse energy to reach the IMT temperature of 68°C, therefore agreeing again with the experimental results in the 200 ps time scale.

Finally, it is valuable to compare the all-optical modulation property of our sample to other active metasurface devices. In ultrafast all-optical modulation experiments, depending on the switching mechanisms, the relative modulation depth has been reported varying from 5 to 30% in literatures [31, 81–84]. For VO_2 materials and photonic devices, this value was usually 10–20% limited by the damaging threshold of VO_2 [29, 65, 81, 82]. However, it is possible to achieve a higher all-optical modulation amplitude by using longer laser pulses or continuous-wave (CW) lasers [29, 65]. As shown in Figure S8 of Supplementary Materials, using CW lasers, we can achieve modulation amplitude comparable to the static heating case in our metasurface sample. Compared to previous reports, our device shows comparable ultrafast modulation amplitude, lower switching power, high transparency and capability for low-cost fabrication. These results indicate a promising potential of using such devices for all-optical switching and modulation applications.

3 Conclusions

In summary, we report a large-scale, power-efficient Au/VO_2-based active metasurfaces for all-optical modulation. By using PS spheres self-assembly, centimeter-scale Au hexagonal periodical nanohole structures were fabricated. By switching on-off the EOT effect using the IMT process of VO_2, we observe a steady state extinction ratio of 12.7 dB

and low insertion loss of 3.3 dB at 2200 nm wavelength in static heating experiment, and $\Delta T/T$ up to 10% in ultrafast pump-probe experiments. Using a femtosecond laser excitation of the SPR mode at 800 nm wavelength, we achieved ultrafast all-optical modulation of the transmittance in the femtosecond to picosecond time scale with 50% power reduction to trigger the IMT process of VO_2. Our work provides a practical way for low-cost fabrication of large-scale and high-performance active metasurfaces based on Au/VO_2 nanostructures.

4 Methods

4.1 Device fabrication

A 90-nm-thick VO_2 film was first deposited by pulsed laser deposition (PLD, TSST) on a quartz substrate with 248 nm KrF excimer laser. The VO_2 film was deposited under 14 mTorr oxygen partial pressure at room temperature. The laser fluence was 3 J cm^{-2}. After deposition, the VO_2 film was *in situ* annealed at 500°C under 1.2 Torr oxygen partial pressure for 1 h. After VO_2 thin film crystallization, the PS sphere was self-assembled on the VO_2 film. The PS spheres were then oxidized by oxygen plasma to reduce the diameter. Then, a 30-nm-thick Au film was sputtered on the sample by magnetron sputtering under 3.7 mTorr Ar partial pressure at a *DC* power 150 W. Finally, the PS sphere was lifted off using ultrasonic cleaning in methylbenzene solution and rinsed in deionized water for 2 min. In order to improve the quality of the Au film, the sample was annealed in furnace at 500°C for 20 min under 100 mTorr oxygen partial pressure.

4.2 Preparation of the monolayer colloidal sphere mask

PS spheres were dispersed in water/ethanol (vol. ratio 1:1) solution with a concentration 15 wt%. For the self-assembly experiment, the solution with 15 wt% PS spheres was slowly dropped onto water surfaces using a pipette. In order to improve a dense self-assembly of PS spheres, a few drops of 0.1 wt% sodium dodecyl sulfate (SDS) were added. After that, the dense packed hexagonal spheres were transferred to the sample surface by slowly pumping out the water. Then, the PS membrane was transferred onto the VO_2 film. Finally, the diameter of PS sphere was downsized from around 550 nm to 400 nm by oxygen plasma.

4.3 Static heating experiment

For temperature control, we used a homemade resistive heater, which can be heated using a temperature controller from room temperature (20 °C) to 100 °C with a resolution of ±0.5 °C. The temperature-dependent transmittance spectrum was measured using a UV-Visible spectrometer (PerkinElmer, Lambda 750). When changing the temperature, a 5 min interval was applied to stabilize the sample temperature between measurements.

Acknowledgments: The authors are grateful for support by the National Natural Science Foundation of China (NSFC) (Grant Nos. 51972044, 11574316, 52021001), Sichuan Provincial Science and Technology Department (Grant No. 2019YFH0154), Ministry of Science and Technology of the People's Republic of China (MOST) (Grant Nos. 2016YFA0300802, 2016YFA0401803, 2018YFE0109200) and Dongguan Introduction Program of Leading Innovative and Entrepreneurial Talents. Ultrafast pump-probe tests were performed on the Steady High Magnetic Field Facilities (Ultrafast optical measurement system under superconducting magnet), High Magnetic Field Laboratory, CAS.

Author contribution: All the authors have accepted responsibility for the entire content of this submitted manuscript and approved submission.

Research funding: The authors are grateful for support by the National Natural Science Foundation of China (NSFC) (Grant Nos. 51972044, 11574316, 52021001), Sichuan Provincial Science and Technology Department (Grant No. 2019YFH0154), Ministry of Science and Technology of the People's Republic of China (MOST) (Grant Nos. 2016YFA0300802, 2016YFA0401803, 2018YFE0109200) and Dongguan Introduction Program of Leading Innovative and Entrepreneurial Talents.

Conflict of interest statement: The authors declare no conflicts of interest regarding this article.

References

[1] M. Lawrence, D. R. Barton, and J. A. Dionne, "Nonreciprocal flat optics with silicon metasurfaces," *Nano Lett.*, vol. 18, no. 2, pp. 1104–1109, 2018.

[2] F. Aieta, P. Genevet, M. A. Kats, et al., "Aberration-free ultrathin flat lenses and axicons at telecom wavelengths based on plasmonic metasurfaces," *Nano Lett.*, vol. 12, no. 9, pp. 4932–4936, 2012.

[3] S. J. Tan, L. Zhang, D. Zhu, et al., "Plasmonic color palettes for photorealistic printing with aluminum nanostructures," *Nano Lett.*, vol. 14, no. 7, pp. 4023–4029, 2014.

[4] Z. L. Deng, J. Deng, X. Zhuang, et al., "Facile metagrating holograms with broadband and extreme angle tolerance," *Light Sci. Appl.*, vol. 7, no. 1, p. 78, 2018.

[5] C. Wan, E. H. Horak, J. King, et al., "Limiting optical diodes enabled by the phase transition of vanadium dioxide," *ACS Photonics*, vol. 5, no. 7, pp. 2688–2692, 2018.

[6] S. Sun, K. Yang, C. Wang, et al., "High-efficiency broadband anomalous reflection by gradient meta-surfaces," *Nano Lett.*, vol. 12, no. 12, pp. 6223–6229, 2012.

[7] U. Zywietz, A. B. Evlyukhin, C. Reinhardt, and B. N. Chichkov, "Laser printing of silicon nanoparticles with resonant optical electric and magnetic responses," *Nat. Commun.*, vol. 5, p. 3402, 2014.

[8] N. Yu, F. Aieta, P. Genevet, et al., "A broadband, background-free quarter-wave plate based on plasmonic metasurfaces," *Nano Lett.*, vol. 12, no. 12, pp. 6328–6333, 2012.
[9] N. Yu, P. Genevet, M. A. Kats, et al., "Light propagation with phase discontinuities: generalized laws of reflection and refraction," *Science*, vol. 334, no. October, pp. 333–337, 2011.
[10] R. Blanchard, G. Aoust, P. Genevet, et al., "Modeling nanoscale V-shaped antennas for the design of optical phased arrays," *Phys. Rev. B*, vol. 85, no. 15, p. 155457, 2012.
[11] E. Arbabi, A. Arbabi, S. M. Kamali, et al., "MEMS-tunable dielectric metasurface lens," *Nat. Commun.*, vol. 9, no. 1, p. 812, 2018.
[12] A. M. Mahmoud, A. R. Davoyan, and N. Engheta, "All-passive nonreciprocal metastructure," *Nat. Commun.*, vol. 6, p. 8359, 2015.
[13] L. Wang, S. Kruk, H. Tang, et al., "Grayscale transparent metasurface holograms," *Optica*, vol. 3, no. 12, pp. 1504–1505, 2016.
[14] W. Wan, J. Gao, and X. Yang, "Full-color plasmonic metasurface holograms," *ACS Nano*, vol. 10, no. 12, pp. 10671–10680, 2016.
[15] T. Li, Q. Wei, B. Reineke, et al., "Reconfigurable metasurface hologram by utilizing addressable dynamic pixels," *Opt. Express*, vol. 27, no. 15, p. 21153, 2019.
[16] Q. Wang, E. Plum, Q. Yang, et al., "Reflective chiral meta-holography: multiplexing holograms for circularly polarized waves," *Light Sci. Appl.*, vol. 7, no. 1, p. 25, 2018.
[17] B. Wang, F. Dong, Q. T. Li, et al., "Visible-frequency dielectric metasurfaces for multiwavelength achromatic and highly dispersive holograms," *Nano Lett.*, vol. 16, no. 8, pp. 5235–5240, 2016.
[18] M. Jang, Y. Horie, A. Shibukawa, et al., "Wavefront shaping with disorder-engineered metasurfaces," *Nat. Photonics*, vol. 12, no. 2, pp. 84–90, 2018.
[19] L. Wang, S. Kruk, K. Koshelev, et al., "Nonlinear wavefront control with all-dielectric metasurfaces," *Nano Lett.*, vol. 18, no. 6, pp. 3978–3984, 2018.
[20] A. Pors, M. G. Nielsen, T. Bernardin, J. C. Weeber, and S. I. Bozhevolnyi, "Efficient unidirectional polarization-controlled excitation of surface plasmon polaritons," *Light Sci. Appl.*, vol. 3, no. 8, p. e197, 2014.
[21] S. Sun, Q. He, J. Hao, S. Xiao, and L. Zhou, "Electromagnetic metasurfaces: physics and applications," *Adv. Opt. Photonics*, vol. 11, no. 2, p. 380, 2019.
[22] S. Sun, Q. He, S. Xiao, et al., "Gradient-index meta-surfaces as a bridge linking propagating waves and surface waves," *Nat. Mater.*, vol. 11, no. 5, pp. 426–431, 2012.
[23] L. Huang, X. Chen, B. Bai, et al., "Helicity dependent directional surface plasmon polariton excitation using a metasurface with interfacial phase discontinuity," *Light Sci. Appl.*, vol. 2, no. 3, p. e70, 2013.
[24] J. Duan, H. Guo, S. Dong, et al., "High-efficiency chirality-modulated spoof surface plasmon meta-coupler," *Sci. Rep.*, vol. 7, no. 1, p. 1354, 2017.
[25] Y. Yao, R. Shankar, M. A. Kats, et al., "Electrically tunable metasurface perfect absorbers for ultrathin mid-infrared optical modulators," *Nano Lett.*, vol. 14, no. 11, pp. 6526–6532, 2014.
[26] G. Kafaie Shirmanesh, R. Sokhoyan, R. A. Pala, and H. A. Atwater, "Dual-gated active metasurface at 1550 nm with wide (>300°) phase tunability," *Nano Lett.*, vol. 18, no. 5, pp. 2957–2963, 2018.
[27] Y. Zhang, C. T. Wang, X. Liang, et al., "Enhanced magneto-optical effect in $Y_{1.5}Ce_{1.5}Fe_5O_{12}$ thin films deposited on silicon by pulsed laser deposition," *J. Alloys Compd.*, vol. 703, pp. 591–599, 2017.
[28] J. Sautter, I. Staude, M. Decker, et al., "Active tuning of all-dielectric metasurfaces," *ACS Nano*, vol. 9, no. 4, pp. 4308–4315, 2015.
[29] D. Y. Lei, K. Appavoo, F. Ligmajer, et al., "Optically-triggered nanoscale memory effect in a hybrid plasmonic-phase changing nanostructure," *ACS Photonics*, vol. 2, no. 9, pp. 1306–1313, 2015.
[30] M. Z. Alam, I. De Leon, and R. W. Boyd, "Large optical nonlinearity of indium tin oxide in its epsilon-near-zero region," *Science*, vol. 352, no. 6287, pp. 795–797, 2016.
[31] P. Guo, R. D. Schaller, L. E. Ocola, et al., "Large optical nonlinearity of ITO nanorods for sub-picosecond all-optical modulation of the full-visible spectrum," *Nat. Commun.*, vol. 7, p. 12892, 2016.
[32] Z. Zhu, P. G. Evans, R. F. Haglund, and J. G. Valentine, "Dynamically reconfigurable metadevice employing nanostructured phase-change materials," *Nano Lett.*, vol. 17, no. 8, pp. 4881–4885, 2017.
[33] C. R. de Galarreta, A. M. Alexeev, Y. Y. Au, et al., "Nonvolatile reconfigurable phase-change metadevices for beam steering in the near infrared," *Adv. Funct. Mater.*, vol. 28, no. 10, p. 1704993, 2018.
[34] Y. W. Huang, H. W. H. Lee, R. Sokhoyan, et al., "Gate-tunable conducting oxide metasurfaces," *Nano Lett.*, vol. 16, no. 9, pp. 5319–5325, 2016.
[35] A. Forouzmand, M. M. Salary, S. Inampudi, and H. Mosallaei, "A tunable multigate indium-tin-oxide-assisted all-dielectric metasurface," *Adv. Opt. Mater.*, vol. 6, no. 7, p. 1701275, 2018.
[36] S. Q. Li, X. Xu, R. M. Veetil, et al., "Phase-only transmissive spatial light modulator based on tunable dielectric metasurface," *Science*, vol. 364, no. 6445, pp. 1087–1090, 2019.
[37] A. Komar, R. Paniagua-Domínguez, A. Miroshnichenko, et al., "Dynamic beam switching by liquid crystal tunable dielectric metasurfaces," *ACS Photonics*, vol. 5, no. 5, pp. 1742–1748, 2018.
[38] F. Morichetti, S. Zanotto, A. Blancato, et al., "Electrochemical optical actuators: controlling the light through ions," in *2016 18th Int. Conf. Transparent Opt. Networks*, pp. 1–4, 2016.
[39] M. C. Sherrott, P. W. C. Hon, K. T. Fountaine, et al., "Experimental demonstration of >230° phase modulation in gate-tunable graphene-gold reconfigurable mid-infrared metasurfaces," *Nano Lett.*, vol. 17, no. 5, pp. 3027–3034, 2017.
[40] Z. Zhu, P. G. Evans, R. F. Haglund, and J. G. Valentine, "Dynamically reconfigurable metadevice employing nanostructured phase-change materials," *Nano Lett.*, vol. 17, no. 8, pp. 4881–4885, 2017.
[41] Y. Qu, Q. Li, L. Cai, et al., "Thermal camouflage based on the phase-changing material GST," *Light Sci. Appl.*, vol. 7, no. 1, p. 26, 2018.
[42] A. Afridi, J. Canet-Ferrer, L. Philippet, et al., "Electrically driven varifocal silicon metalens," *ACS Photonics*, vol. 5, no. 11, pp. 4497–4503, 2018.
[43] J. He, Z. Xie, W. Sun, et al., "Terahertz tunable metasurface lens based on vanadium dioxide phase transition," *Plasmonics*, vol. 11, no. 5, pp. 1285–1290, 2016.
[44] C. Ríos, P. Hosseini, R. A. Taylor, and H. Bhaskaran, "Color depth modulation and resolution in phase-change material

nanodisplays," *Adv. Mater.*, vol. 28, no. 23, pp. 4720–4726, 2016.
[45] X. Yin, T. Steinle, L. Huang, et al., "Beam switching and bifocal zoom lensing using active plasmonic metasurfaces," *Light Sci. Appl.*, vol. 6, no. 7, p. e17016–e17016, 2017.
[46] Y. Meng, J. K. Behera, Y. Ke, et al., "Design of a 4-level active photonics phase change switch using VO_2 and Ge2Sb2Te5," *Appl. Phys. Lett.*, vol. 113, no. 7, p. 071901, 2018.
[47] K. V. Sreekanth, S. Han, and R. Singh, "Ge2Sb2Te5-based tunable perfect absorber cavity with phase singularity at visible frequencies," *Adv. Mater.*, vol. 30, no. 21, p. 1706696, 2018.
[48] N. Mou, X. Liu, T. Wei, et al., "Large-scale, low-cost, broadband and tunable perfect optical absorber based on phase-change material," *Nanoscale*, vol. 12, no. 9, pp. 5374–5379, 2020.
[49] M. A. Kats, R. Blanchard, S. Zhang, et al., "Vanadium dioxide as a natural disordered metamaterial: perfect thermal emission and large broadband negative differential thermal emittance," *Phys. Rev. X*, vol. 3, no. 4, p. 041004, 2013.
[50] D. Wegkamp, M. Herzog, L. Xian, et al., "Instantaneous band gap collapse in photoexcited monoclinic VO_2 due to photocarrier doping," *Phys. Rev. Lett.*, vol. 113, no. 21, p. 216401, 2014.
[51] V. R. Morrison, R. P. Chatelain, K. L. Tiwari, et al., "A photoinduced metal-like phase of monoclinic VO_2 revealed by ultrafast electron diffraction," *Science*, vol. 346, no. 6208, pp. 445–448, 2014.
[52] M. R. Otto, L. P. René de Cotret, D. A. Valverde-Chavez, et al., "How optical excitation controls the structure and properties of vanadium dioxide," *Proc. Natl. Acad. Sci. U. S. A*, vol. 116, no. 2, pp. 450–455, 2019.
[53] M. F. Jager, C. Ott, P. M. Kraus, et al., "Tracking the insulator-to-metal phase transition in VO_2 with few-femtosecond extreme UV transient absorption spectroscopy," *Proc. Natl. Acad. Sci. U. S. A*, vol. 114, no. 36, pp. 9558–9563, 2017.
[54] J. Y. Suh, E. U. Donev, R. Lopez, L. C. Feldman, and R. F. Haglund, "Modulated optical transmission of subwavelength hole arrays in metal-VO_2 films," *Appl. Phys. Lett.*, vol. 88, no. 13, p. 133115, 2006.
[55] X. Xu, X. He, H. Wang, et al., "The extremely narrow hysteresis width of phase transition in nanocrystalline VO_2 thin films with the flake grain structures," *Appl. Surf. Sci.*, vol. 261, pp. 83–87, 2012.
[56] Y. Li, J. Li, T. Huang, et al., "Active macroscale visible plasmonic nanorod self-assembled monolayer," *Photonics Res.*, vol. 6, no. 5, p. 409, 2018.
[57] Z. Y. Jia, F. Z. Shu, Y. J. Gao, et al., "Dynamically switching the polarization state of light based on the phase transition of vanadium dioxide," *Phys. Rev. Appl.*, vol. 9, no. 3, p. 34009, 2018.
[58] M. A. Kats, R. Blanchard, P. Genevet, et al., "Thermal tuning of mid-infrared plasmonic antenna arrays using a phase change material," *Opt. Lett.*, vol. 38, no. 3, pp. 368–370, 2013.
[59] M. Sun, M. Taha, S. Walia, et al., "A photonic switch based on a hybrid combination of metallic nanoholes and phase-change vanadium dioxide," *Sci. Rep.*, vol. 8, p. 11106, 2018.
[60] Y. G. Jeong, S. Han, J. Rhie, et al., "A vanadium dioxide metamaterial disengaged from insulator-to-metal transition," *Nano Lett.*, vol. 15, no. 10, pp. 6318–6323, 2015.
[61] L. Liu, L. Kang, T. S. Mayer, and D. H. Werner, "Hybrid metamaterials for electrically triggered multifunctional control," *Nat. Commun.*, vol. 7, p. 13236, 2016.
[62] F. Z. Shu, F. F. Yu, R. W. Peng, et al., "Dynamic plasmonic color generation based on phase transition of vanadium dioxide," *Adv. Opt. Mater.*, vol. 6, no. 7, p. 1700939, 2018.
[63] S. Chandra, D. Franklin, J. Cozart, A. Safaei, and D. Chanda, "Adaptive multispectral infrared camouflage," *ACS Photonics*, vol. 5, no. 11, pp. 4513–4519, 2018.
[64] K. Appavoo, B. Wang, N. F. Brady, et al., "Ultrafast phase transition via catastrophic phonon collapse driven by plasmonic hot-electron injection," *Nano Lett.*, vol. 14, no. 3, pp. 1127–1133, 2014.
[65] O. L. Muskens, L. Bergamini, Y. Wang, et al., "Antenna-assisted picosecond control of nanoscale phase transition in vanadium dioxide," *Light Sci. Appl.*, vol. 5, no. 10, p. e16173, 2016.
[66] T. D. Dao, K. Chen, S. Ishii, et al., "Infrared perfect absorbers fabricated by colloidal mask etching of Al-Al_2O_3-Al trilayers," *ACS Photonics*, vol. 2, no. 7, pp. 964–970, 2015.
[67] S. G. Rodrigo, F. J. García-Vidal, and L. Martín-Moreno, "Influence of material properties on extraordinary optical transmission through hole arrays," *Phys. Rev. B*, vol. 77, no. 7, 2008, p. 075401.
[68] A. Degiron, H. J. Lezec, W. L. Barnes, and T. W. Ebbesen, "Effects of hole depth on enhanced light transmission through subwavelength hole arrays," *Appl. Phys. Lett.*, vol. 81, no. 23, pp. 4327–4329, 2002.
[69] N. Bonod, S. Enoch, L. Li, E. Popov, and M. Neviere, "Resonant optical transmission through thin metallic films with and without holes," *Opt. Express*, vol. 11, no. 5, pp. 482–490, 2003.
[70] S. G. Rodrigo, F. De León-Pérez, and L. Martin-Moreno, "Extraordinary optical transmission: fundamentals and applications," *Proc. IEEE*, vol. 104, no. 12, pp. 2288–2306, 2016.
[71] T. W. Ebbesen, H. J. Lezec, H. F. Ghaemi, T. Thio, and P. A. Wolff, "Extraordinary optical transmission through sub-wavelength hole arrays," *Nature*, vol. 391, no. 6668, pp. 667–669, 1998.
[72] K. L. Van Der Molen, K. J. Klein Koerkamp, S. Enoch, et al., "Role of shape and localized resonances in extraordinary transmission through periodic arrays of subwavelength holes: experiment and theory," *Phys. Rev. B*, vol. 72, p. 045421, no. 4, 2005.
[73] J. Han, A. K. Azad, M. Gong, X. Lu, and W. Zhang, "Coupling between surface plasmons and nonresonant transmission in subwavelength holes at terahertz frequencies," *Appl. Phys. Lett.*, vol. 91, no. 7, p. 071122, 2007.
[74] J. Braun, B. Gompf, G. Kobiela, and M. Dressel, "How holes can obscure the view: suppressed transmission through an ultrathin metal film by a subwavelength hole array," *Phys. Rev. Lett.*, vol. 103, no. 20, p. 203901, 2009.
[75] J. Y. Li, Y. L. Hua, J. X. Fu, and Z. Y. Li, "Influence of hole geometry and lattice constant on extraordinary optical transmission through subwavelength hole arrays in metal films," *J. Appl. Phys.*, vol. 107, no. 7, p. 073101, 2010.
[76] H. Liu and P. Lalanne, "Microscopic theory of the extraordinary optical transmission," *Nature*, vol. 452, no. 7188, pp. 728–731, 2008.
[77] J. M. McMahon, J. Henzie, T. W. Odom, G. C. Schatz, and S. K. Gray, "Tailoring the sensing capabilities of nanohole arrays in gold films with Rayleigh anomaly-surface plasmon polaritons," *Opt. Express*, vol. 15, no. 26, pp. 18119–18129, 2007.
[78] Z. Shao, X. Cao, H. Luo, and P. Jin, "Recent progress in the phase-transition mechanism and modulation of vanadium dioxide materials," *NPG Asia Mater.*, vol. 10, no. 7, pp. 581–605, 2018.
[79] S. Wall, L. Foglia, D. Wegkamp, et al., "Tracking the evolution of electronic and structural properties of VO_2 during the ultrafast

photoinduced insulator-metal transition," *Phys. Rev. B*, vol. 87, no. 11, p. 115126, 2013.

[80] M. Hada, D. Zhang, A. Casandruc, et al., "Hot electron injection driven phase transitions," *Phys. Rev. B*, vol. 86, no. 13, pp. 1–6, 2012.

[81] P. Guo, M. S. Weimer, J. D. Emery, et al., "Conformal coating of a phase change material on ordered plasmonic nanorod arrays for broadband all-optical switching," *ACS Nano*, vol. 11, no. 1, pp. 693–701, 2017.

[82] N. Kumar, A. Rúa, J. Aldama, et al., "Photoinduced surface plasmon switching at VO_2/Au interface," *Opt. Express*, vol. 26, no. 11, p. 13773, 2018.

[83] K. Wang, L. Chen, H. Zhang, and J. Chen, "Controlling surface plasmon polaritons at femtosecond timescales on an aluminum-coated grating," *Appl. Phys. Lett.*, vol. 110, no. 2, p. 021105, 2017.

[84] X. Zhang, B. Sun, J. M. Hodgkiss, and R. H. Friend, "Tunable ultrafast optical switching via waveguided gold nanowires," *Adv. Mater.*, vol. 20, no. 23, pp. 4455–4459, 2008.

Supplementary Material: The online version of this article offers supplementary material (https://doi.org/10.1515/nanoph-2020-0354).